

Abundance matching with the mean star formation rate: there is no missing satellites problem in the Milky Way

J. I. Read^{1*}, D. Erkal¹

¹*Department of Physics, University of Surrey, Guildford, GU2 7XH, UK*

20 July 2018

ABSTRACT

Classical abundance matching statistically links the stellar mass of galaxies, M_* , to their halo masses, M_{200} , in a given cosmological model. For isolated dwarf galaxies, assuming a Λ CDM cosmology, this has been shown to produce mass estimates, M_{200}^{abund} , that agree well with independent dynamical estimates, M_{200}^{dyn} . However, for satellite galaxies, classical abundance matching is expected to fail. This is because tidal stripping lowers M_* and M_{200}^{dyn} , causing satellites to scatter above the $M_* - M_{200}$ relation for isolated dwarfs, while ram-pressure stripping quenches star formation on infall, causing satellites to scatter below the relation.

In this paper, we introduce a novel abundance matching technique that produces a more accurate estimate of M_{200} for satellite galaxies. To achieve this, we abundance match with the mean star formation rate, averaged over the time when a galaxy was forming stars, $\langle \text{SFR} \rangle$, instead of M_* . Using data from the Sloan Digital Sky Survey and the Bolshoi simulation, we obtain a statistical $\langle \text{SFR} \rangle - M_{200}$ relation in Λ CDM. We then compare M_{200}^{abund} derived from this relation with M_{200}^{dyn} for 21 nearby dSph and dIrr galaxies, finding a good agreement between the two.

As a first application, we use our new $\langle \text{SFR} \rangle - M_{200}$ relation to empirically measure the cumulative mass function of a volume-complete sample of bright Milky Way satellites within 280 kpc of the Galactic centre. We compare this with a suite of cosmological ‘zoom’ simulations of Milky Way-mass halos that account for subhalo depletion by the Milky Way disc. Including a conservative lower bound on the number of ‘ultra-faint’ dwarfs in this same volume, we find no missing satellites problem above $M_{200} \sim 10^9 M_\odot$ in the Milky Way. We discuss how this empirical method can be applied to a larger sample of spiral galaxies in the Local Volume.

Key words:

1 INTRODUCTION

The standard Λ CDM cosmological model makes concrete predictions for the growth of dark matter structure over cosmic time (e.g. White & Rees 1978; Frenk et al. 1988). This produces an excellent description of the distribution of mass in the Universe on large scales ($\gtrsim 10$ Mpc) (e.g. Springel et al. 2006; Percival 2013). However, on smaller scales there have been long-standing tensions. Key amongst these is the “missing satellites problem” (Moore et al. 1999; Klypin et al. 1999). Pure dark matter structure formation simulations predict many more bound dark matter halos than visible satellites around the Milky Way and M31 (and see e.g. Bullock & Boylan-Kolchin 2017, for a review). Despite the re-

cent explosion in the numbers of dwarf galaxies found by large surveys (e.g. Belokurov et al. 2007; Ibata et al. 2007; McConnachie 2012; Bechtol et al. 2015; Drlica-Wagner et al. 2015; Koposov et al. 2015), this problem still persists today (e.g. Koposov et al. 2008; Tollerud et al. 2008).

Reasonable assumptions about galaxy formation can be made that will solve the missing satellites problem, typically by assuming that some subhalos light up with stars while others remain dark (e.g. Macciò et al. 2010; Sawala et al. 2016). However, even the latest galaxy formation simulations find very different results at the scale of dwarf galaxies (e.g. Mayer et al. 2008; Scannapieco et al. 2012; Contenta et al. 2017). As a result, many proposed solutions to the missing satellites problem disagree in the details. Some are unable to simultaneously produce the mass function and radial distribution of the satellites (e.g. Koposov et al. 2008),

* E-mail: justin.inglis.read@gmail.com

or their internal kinematics (e.g. Read et al. 2006b; Boylan-Kolchin et al. 2011); some are even mutually exclusive, relying on the formation of dark matter cores due to bursty stellar feedback (e.g. Zolotov et al. 2012; Wetzel et al. 2016), or not requiring this at all (e.g. Sawala et al. 2016; Fattahi et al. 2016).

Each of the above solutions places the Milky Way satellites in different pre-infall dark matter halos. Thus, an empirical method for mapping visible galaxies to dark matter halos would allow us to determine which, if any, of the above models is correct. This is the goal of ‘abundance matching’. In its simplest form, abundance matching statistically maps galaxies of an observed number density in the Universe to dark matter halos of the same number density selected from a cosmological N -body simulation (e.g. Peacock & Smith 2000; Kravtsov et al. 2004; Vale & Ostriker 2004, 2006). From this mapping, we can then derive a statistical relationship between some galaxy property, \mathcal{G} , and its dark matter halo mass, M_{200} . Although \mathcal{G} is usually taken to be the stellar mass of galaxy, M_* , abundance matching can be used to link *any* galaxy property to halo mass, so long as the property in question rises monotonically with M_{200} , and has negligible scatter.

Once a statistical relationship between \mathcal{G} and M_{200} has been established, we can compare this with direct measurements of \mathcal{G} and M_{200} to probe cosmological models and test galaxy formation theories. This has the advantage that, while \mathcal{G} must be measured for a large sample of galaxies that have a known selection function, M_{200} – which is much harder to estimate – need only be inferred for a subset of galaxies with excellent quality data. To date, this sort of comparison has only been performed using stellar masses ($\mathcal{G} \equiv M_*$) obtained from Spectral Energy Distribution (SED) model fitting (e.g. Wuyts et al. 2009; Walcher et al. 2011; Mitchell et al. 2013) and M_{200} obtained from either gravitational lensing, or HI rotation curves (e.g. Mandelbaum et al. 2006; Moster et al. 2010; Kravtsov et al. 2014; Read et al. 2017; Katz et al. 2017). These studies find that Λ CDM gives a good representation of the data over an impressive mass range of $5 \times 10^9 \lesssim M_{200}/M_\odot \lesssim 10^{15}$.

While M_* has been used successfully for abundance matching of isolated ‘central’ galaxies, for satellites it is more problematic. Satellites have their star formation shut down (‘quenched’) on infall to a larger galaxy or group (e.g. Peng et al. 2012; Geha et al. 2012; Gatto et al. 2013). This ‘freezes-in’ their stellar mass, causing them to scatter below the $M_* - M_{200}$ relation for isolated dwarfs (e.g. Ural et al. 2015; Contreras et al. 2015; Read et al. 2017). Satellites also experience mass loss due to tidal stripping and shocking, causing them to scatter above relation (e.g. Read et al. 2006a; Tomozeiu et al. 2016; and see Figure 1). One solution to these problems is to model this scatter statistically as a ‘nuisance’ parameter (e.g. Garrison-Kimmel et al. 2017a; Jethwa et al. 2018). However, this limits our ability to probe cosmological models or test galaxy formation theories. An alternative approach is to directly match satellites to subhalos in numerical simulations (e.g. Madau et al. 2008; Boylan-Kolchin et al. 2012; Brook et al. 2014; Kim et al. 2017). However, again there is some freedom in how to do this (e.g. selecting the halos which are the most massive before infall, the most massive before some redshift, or selecting them stochastically, e.g. Diemand et al. 2007). Fi-

nally, ‘SubHalo Abundance Matching’ (SHAM) methods explicitly model the effect of tides and quenching for satellites in a given cosmology (e.g. Zentner et al. 2005; Hearin et al. 2013), moving us in the direction of ‘semi-analytic’ galaxy formation models (e.g. Baugh 2006). However, as with the other approaches above, this removes the key advantage of classical abundance matching that it is entirely empirical.

In this paper, we present a new abundance matching method that is designed to work equally well for central galaxies and satellites, while retaining a purely empirical mapping between galaxies and their (sub-)halos. The key idea is to abundance match with the *mean star formation rate*, $\langle \text{SFR} \rangle$, of galaxies (averaged over the time during which the galaxy was forming stars) instead of the stellar mass. It has already been shown that, for isolated galaxies, the stellar mass is monotonically related to the halo mass (e.g. Moster et al. 2010; Kravtsov et al. 2014; Read et al. 2017; Katz et al. 2017). Thus, the $\langle \text{SFR} \rangle$ of isolated galaxies, as defined above, must also monotonically rise with M_{200} (see Figure 1). However, as we shall show in this paper, the advantage of using the $\langle \text{SFR} \rangle$ over M_* is that, for satellite galaxies, it has less scatter at a given pre-infall M_{200} , increasing the accuracy of the mass estimator, M_{200}^{abund} .

Our new abundance matching method alleviates the problem of scatter in M_* due to satellite quenching, but does not solve the problem of scatter due to tidal mass loss. We argue, however, that this is only a problem if a satellite loses significant stellar mass. If a satellite loses its outer dark matter halo, this will lower its present-day dynamical mass, M_{200}^{dyn} , but not its abundance matching mass, M_{200}^{abund} , which is a statistical estimate of the *pre-infall* halo mass of the satellite, M_{200} . Furthermore, even significant stellar mass loss due to tides can be corrected for if the satellite has visible tidal tails. This is the case, for example, for the Sagittarius dwarf spheroidal galaxy in the Milky Way (Ibata et al. 1995, 1997; Niederste-Ostholt et al. 2010, 2012).

The goal of this paper is to quantitatively explore our novel abundance matching with the $\langle \text{SFR} \rangle$, with an initial application to a volume-complete sample of bright satellite galaxies within 280 kpc of the centre of the Milky Way. Comparing the cumulative mass function of these, determined from the $\langle \text{SFR} \rangle - M_{200}$ relation, with a suite of cosmological simulations that include the effect of satellite depletion by the disc, we ask afresh whether there is, in fact, a missing satellite problem in the Milky Way in Λ CDM.

This paper is organised as follows. In §2, we describe our $\langle \text{SFR} \rangle - M_{200}$ abundance matching method in more detail (§2.1, §2.2), and we describe our method for obtaining the $\langle \text{SFR} \rangle$ and dynamical M_{200}^{dyn} for a sample of isolated and satellite dwarfs (§2.3). In §3, we describe the data used in this work. In §4, we describe the cosmological ‘zoom’ simulations of Milky Way mass halos that we use in this work to compare with our empirically derived subhalo mass function. In §5 we present our results. In §5.1, we compare M_{200}^{abund} derived from our $\langle \text{SFR} \rangle$ abundance matching with M_{200}^{dyn} for a sample of 11 isolated and 10 satellite dwarfs. In §5.3, we use the $\langle \text{SFR} \rangle - M_{200}$ relation to calculate the cumulative subhalo mass function of the Milky Way. We compare this to the simulations described in §4. In §6, we discuss the caveats and systematic errors inherent in our methodology, the implications of our results for other small scale puzzles

in Λ CDM, and reionisation. Finally, in §7, we present our conclusions.

2 METHOD

In this section, we define the $\langle \text{SFR} \rangle$ for central and satellite galaxies (§2.1); we present our $\langle \text{SFR} \rangle$ abundance matching method (§2.2); and we describe how we obtain stellar masses, M_* , the $\langle \text{SFR} \rangle$, and dynamical masses, M_{200}^{dyn} , for satellite and central dwarf galaxies (§2.3).

2.1 Defining the $\langle \text{SFR} \rangle$ for different galaxy populations

We define the $\langle \text{SFR} \rangle$ as the star formation rate averaged over all times when a galaxy was actively forming stars. However, there are some subtleties to consider when turning this into a practical definition that can be applied to real data. We discuss these next.

2.1.1 Isolated star forming galaxies

For isolated galaxies that have formed stars for a Hubble time, we estimate the mean star formation rate simply from their stellar masses, M_* :

$$\langle \text{SFR} \rangle = \frac{M_*}{t_{\text{univ}}} \quad (1)$$

where $t_{\text{univ}} = 13.8$ Gyrs (e.g. Planck Collaboration et al. 2014). We could also estimate it from an average over the star formation history (SFH) determined from deep colour magnitude diagrams (CMDs), or from SED model fitting (e.g. Walcher et al. 2011; Ruiz-Lara et al. 2015). However, deep CMDs are only available for a few nearby systems. Furthermore, the closest have data for only small portions of the galaxy, requiring an extrapolation to determine the global $\langle \text{SFR} \rangle$ that we require here (e.g. Weisz et al. 2014; Bermejo-Clement et al. 2018). Similarly, while SFHs determined from SED fitting are available for a much larger sample of galaxies, the errors on the $\langle \text{SFR} \rangle$, determined in this way, are substantially larger than the errors on M_* (e.g. Zhang et al. 2012). For these reasons, we use equation 1 for isolated galaxies, assuming an error on M_* (and therefore on our derived $\langle \text{SFR} \rangle$) of 25% (e.g. Mobasher et al. 2015).

2.1.2 Quenched satellite galaxies

For quenched satellite galaxies, we define the $\langle \text{SFR} \rangle$ for our satellite sample to be the SFR averaged over all times when the $\text{SFR}(t) > \max[\text{SFR}]/3$:

$$\langle \text{SFR} \rangle = \frac{\int_0^{t_{\text{univ}}} f \cdot \text{SFR}(t) dt}{\int_0^{t_{\text{univ}}} f dt} \quad (2)$$

where:

$$f(t) = \begin{cases} 1 & \text{if } \text{SFR}(t) > \max[\text{SFR}]/3 \\ 0 & \text{otherwise} \end{cases} \quad (3)$$

This cut is chosen to avoid the $\langle \text{SFR} \rangle$ being biased low by periods where the SFR is slowly declining due to quenching. Choosing to cut instead on $\max[\text{SFR}]/2$ or $\max[\text{SFR}]/4$ shifts our estimates of M_{200}^{abund} for the satellites by less than their 68% confidence intervals.

We ensure that $\text{SFR}(t)$ is normalised such that:

$$\int_0^{t_{\text{univ}}} \text{SFR}(t) dt = M_* \quad (4)$$

In this way, we only use the SFHs to determine *when* star formation is quenched. Thus, the error on the $\langle \text{SFR} \rangle$ is still determined primarily by the error on M_* . We take this to be 25%, as for our isolated star forming galaxies.

2.1.3 Massive ‘self-quenched’ galaxies

Finally, massive galaxies can self-quench independently of environment (e.g. Peng et al. 2010). For these, we should use the $\langle \text{SFR} \rangle$ averaged over the total star formation time, as we do for quenched satellites. However, any quenching that owes entirely to the mass of a galaxy will not break the monotonic relationship between M_* and M_{200} . Indeed, this is why abundance matching with M_* works well for massive galaxies, whether quenched or not (e.g. Kravtsov et al. 2014). For this reason, we use equation 1 also for massive quenched galaxies.

2.2 Abundance matching with the $\langle \text{SFR} \rangle$

To abundance match with the $\langle \text{SFR} \rangle$, we first need a large sample of galaxies with a known selection function and a well-measured $\langle \text{SFR} \rangle$. From these, we can calculate the $\langle \text{SFR} \rangle$ mass function – i.e. the cumulative number density of galaxies, normalised to 1 Mpc^3 , as a function of their $\langle \text{SFR} \rangle$. For this task, we use the Blanton et al. (2005) survey of low luminosity galaxies that had their stellar masses calculated by Baldry et al. (2008) (and see also Behroozi et al. 2013). This is complete to a stellar mass of $M_* \sim 2 \times 10^7 M_{\odot}$ over a volume of $\sim 2 \times 10^6 \text{ Mpc}^3$. (In Appendix A, we show that this stellar mass function is in excellent agreement with the more recent measurement from the GAMA survey (Wright et al. 2017).)

To be fully self-consistent with our definition of the $\langle \text{SFR} \rangle$ above, we should separate galaxies into ‘centrals’ and ‘satellites’, applying equation 1 to the centrals and equation 2 to the satellites. However, over the large volume of data that we use here, quenched satellites are a small fraction of the total number density of galaxies at all stellar masses (e.g. Peng et al. 2012). Thus, to a very good approximation, we can simply use equation 1. This makes calculating the $\langle \text{SFR} \rangle - M_{200}$ particularly straightforward. We simply take the $M_* - M_{200}$ relation derived in Read et al. (2017) (Figure 1 (left)) and divide the stellar masses through by t_{univ} . This is shown by the solid blue lines in Figure 1 (right).

Finally, we would ultimately like to use the $\langle \text{SFR} \rangle - M_{200}$ relation to determine M_{200}^{abund} for satellite galaxies of a given $\langle \text{SFR} \rangle$. We may worry, however, about the effect of the time evolution of the $\langle \text{SFR} \rangle - M_{200}$ relation. For satellites that quench when the Universe is substantially younger, we should use the $\langle \text{SFR} \rangle - M_{200}$ relation *at the time of quenching* to obtain M_{200}^{abund} , rather than that

measured today. In Appendix B we use data from Behroozi et al. (2013) to measure the $\langle\text{SFR}\rangle$ – M_{200} relation as a function of time. For the dwarf galaxies that we are interested in in this paper, we show that this time evolution is not likely to be important for redshifts $z < 3$, corresponding to a look-back time in ΛCDM of $t_{\text{age}} = 11.4$ Gyrs. For more massive quenched galaxies that may be found in cluster environments, however, the time-evolution of the $\langle\text{SFR}\rangle$ – M_{200} relation should be taken into account. As a further test of this, in Appendix C we apply our $\langle\text{SFR}\rangle$ – M_{200} relation to four nearby dwarfs with extended star formation (Fornax, WLM, Aquarius and Carina). For each of these dwarfs, we *artificially* truncate their star formation at different times $t_{\text{trunc}} < 10$ Gyrs to mimic the effect of star formation ceasing on infall to the Milky Way. We find that, within a factor ~ 2 , we obtain a consistent M_{200}^{abund} for these galaxies independently of t_{trunc} . This gives us confidence that we can use the $\langle\text{SFR}\rangle$ – M_{200} relation on nearby quenched satellites whose star formation shut down long ago. We test this further in §5.1 where we compare M_{200}^{abund} derived from the $\langle\text{SFR}\rangle$ – M_{200} relation to M_{200}^{dyn} calculated from stellar and gas kinematics for 21 nearby dwarf galaxies.

2.3 Determining M_* , $\langle\text{SFR}\rangle$ and M_{200}^{dyn} for isolated and satellite dwarfs

To assess the validity of our $\langle\text{SFR}\rangle$ – M_{200} relation, in §5 we compare it with measurements of the $\langle\text{SFR}\rangle$ and M_{200}^{dyn} for nearby dwarf galaxies. In this section, we describe our method for obtaining M_* , $\langle\text{SFR}\rangle$ and M_{200}^{dyn} for these dwarfs.

For M_* , we use the values reported in Read et al. (2017) for the isolated dwarf sample (which are taken from Zhang et al. 2012), and those in McConnachie (2012) for the satellite dwarfs. These are reported in Table 1. For the $\langle\text{SFR}\rangle$, we use equation 1 for our isolated dwarfs and equation 2 for the quenched satellites. The SFH data that we use, and our derived $\langle\text{SFR}\rangle$, are given in §3 and Table 1.

We obtain M_{200}^{dyn} for the gas rich isolated dwarfs from their HI rotation curves as in Read et al. (2017); we refer the reader to that paper for details of the methodology and a data table of M_{200}^{dyn} for our sample of isolated dwarfs. For the LMC and Sagittarius, we use M_{200}^{dyn} values from the literature. The pre-infall halo mass of the LMC was recently estimated by Peñarrubia et al. (2016) using a timing argument. They found $M_{200,\text{LMC}} = 0.25_{-0.08}^{+0.09} \times 10^{12} M_{\odot}$. The Sagittarius dwarf’s pre-infall M_{200}^{dyn} was estimated by Gibbons et al. (2017) from the kinematics of its stellar stream stars. They found $M_{200,\text{Sag}} > 6 \times 10^{10} M_{\odot}$. These values are reported in Table 1.

For the remainder of the Milky Way classical dwarfs, we calculate M_{200}^{dyn} by mass modelling them with the GRAVSPHERE code. GRAVSPHERE is described and tested in detail in Read & Steger (2017) and Read et al. (2018). Here, we use the code as in Read et al. (2018) where the dark matter mass profile is given by the CORENFWTIDES model:

$$\rho_{\text{cNFWt}}(r) = \begin{cases} \rho_{\text{cNFW}} & r < r_t \\ \rho_{\text{cNFW}}(r_t) \left(\frac{r}{r_t}\right)^{-\delta} & r > r_t \end{cases} \quad (5)$$

where ρ_{cNFW} is given by:

$$\rho_{\text{cNFWt}}(r) = f^n \rho_{\text{NFW}} + \frac{nf^{n-1}(1-f^2)}{4\pi r^2 r_c} M_{\text{NFW}} \quad (6)$$

and ρ_{NFW} and M_{NFW} are the ‘NFW’ density and mass profile given by (Navarro et al. 1996b):

$$\rho_{\text{NFW}}(r) = \rho_0 \left(\frac{r}{r_s}\right)^{-1} \left(1 + \frac{r}{r_s}\right)^{-2} \quad (7)$$

$$M_{\text{NFW}}(r) = M_{200} g_c \left[\ln \left(1 + \frac{r}{r_s}\right) - \frac{r}{r_s} \left(1 + \frac{r}{r_s}\right)^{-1} \right] \quad (8)$$

with scale length r_s :

$$r_s = r_{200}/c_{200} \quad (9)$$

where:

$$g_c = \frac{1}{\log(1 + c_{200}) - \frac{c_{200}}{1 + c_{200}}} \quad (10)$$

and:

$$r_{200} = \left[\frac{3}{4} M_{200} \frac{1}{\pi \Delta \rho_{\text{crit}}} \right]^{1/3} \quad (11)$$

where c_{200} is the ‘concentration parameter’, $\Delta = 200$, $\rho_{\text{crit}} = 136.05 M_{\odot} \text{ kpc}^{-3}$ is the critical density of the Universe at redshift $z = 0$, r_{200} is the virial radius, and M_{200} is the virial mass.

The CORENFWTIDES model has six free parameters: M_{200} and c_{200} that are identical to the free parameters in the NFW model, r_c that controls the size of the central dark matter core, n that controls the inner logarithmic slope of the density profile ($n = 0$ is maximally cored, while $n = 1$ reverts to a cusped NFW profile), and r_t and δ that set the radius and outer density slope beyond which mass is tidally stripped from the galaxy, respectively. The CORENFWTIDES model allows us to fit directly for M_{200} while allowing for a central dark matter core and/or some outer steepening of the density profile dues to tides, should the data warrant it. The only difference between the application of the CORENFWTIDES model to Draco in Read et al. (2018) and our analysis here is that in this paper we use slightly more generous priors on M_{200} and c_{200} : $8.5 < \log_{10}(M_{200}/M_{\odot}) < 10.5$; $9 < c_{200} < 24$; $-2 < \log_{10}(r_c/\text{kpc}) < 0.5$; $2 < \log_{10}(r_t/R_{1/2}) < 50$; and $3.5 < \delta < 5$. This is because we found that some of the dwarfs were pushing on the lower bound of the priors on M_{200} used in Read et al. (2018). As in Read et al. (2018), we fix $n = 0$.

3 THE DATA

In this section, we describe the data used in this work. We construct the $\langle\text{SFR}\rangle$ – M_{200} relation using the Blanton et al. (2005) survey of low luminosity galaxies that had their stellar masses calculated by Baldry et al. (2008), as described in §2.2. To test this relation, we compare it to measurements of $\langle\text{SFR}\rangle$ and M_{200}^{dyn} for a sample of nearby dwarf galaxies. The 11 dwarf irregular galaxies are taken from Read et al. (2017) and are described in detail in that paper. We calculate $\langle\text{SFR}\rangle$ for this sample of dIrrs as described in §2.3. The satellite dwarf sample comprises the eight Milky Way

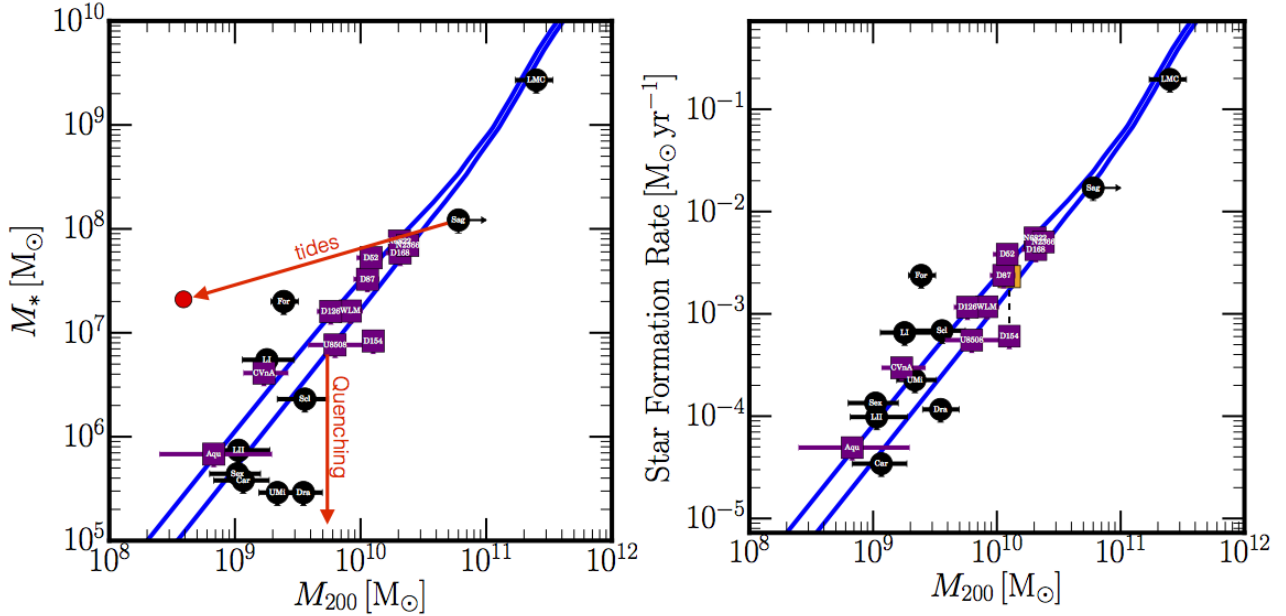


Figure 1. Abundance matching with the stellar mass, M_* (left), and the mean star formation rate, $\langle \text{SFR} \rangle$ (right). The blue lines show the $M_* - M_{200}$ relation from Read et al. (2017) (left) and the $\langle \text{SFR} \rangle - M_{200}$ relation, derived as described in §2.2 (right). The purple data points show isolated dIrrs with M_{200}^{dyn} derived from their HI rotation curves (Read et al. 2017) and $\langle \text{SFR} \rangle$ derived from their stellar masses (equation 1). The black data points show satellite dwarfs. These have their M_{200}^{dyn} and $\langle \text{SFR} \rangle$ determined as described in §2.3 (and see Table 1). Notice that most of the satellites scatter below the $M_* - M_{200}$ relation (left); this owes to satellite quenching (red arrow, as marked). Fornax, however, lies above the relation, indicative of tidal stripping (see red arrow, as marked). Indeed, the present-day M_* and M_{200}^{dyn} for the Sagittarius dwarf (red) are significantly lower than estimates of its pre-infall M_* and M_{200}^{dyn} that utilise data from its tidal tails (black data point marked ‘Sag’, and see text for further details). The orange square, connected to DDO 154 by a dashed line in the right-panel, shows the location of DDO 154 if its *current* SFR is used instead of its Hubble time averaged $\langle \text{SFR} \rangle$ (see text for further details).

‘classical’ dwarf spheroidals (dSphs): Draco, Fornax, UMi, Carina, Sextans, Sculptor, Leo I, and Leo II, the Sagittarius dSph, and the Large Magellanic Cloud (LMC) that is a dwarf irregular (dIrr). Our method for calculating M_{200}^{dyn} for this sample is described in §2.3. The stellar kinematic and photometric data required for mass modelling the classical dwarfs are taken from: Walker et al. (2009a) for Carina, Fornax, Sculptor and Sextans; Mateo et al. (2008) for Leo I; Spencer et al. (2017) for Leo II; Walker et al. (2015) for Draco; and Spencer et al., in prep. for Ursa Minor. The membership selection criteria and determination of the photometric light profiles for these galaxies is described in detail in (Read et al., in prep. 2018).

To calculate the $\langle \text{SFR} \rangle$ for the above sample of galaxies, we require their star formation histories and stellar masses. For galaxies with continuing star formation today, we calculate $\langle \text{SFR} \rangle$ using equation 1 (see §2.3). We take stellar masses for the dIrr sample from Zhang et al. (2012) as in Read et al. (2017). For the sample of nearby satellite galaxies, we take M_* from the McConnachie (2012) review. In both cases, we assume errors on M_* of 25% (e.g. Mobasher et al. 2015). For the quenched satellites, we require also their star formation histories. For these, we use literature determinations derived from deep resolved colour magnitude diagrams (Draco, Aparicio et al. 2001; Sculptor, de Boer et al. 2012a; Carina, de Boer et al. 2014; Fornax, de Boer et al. 2012b; Sextans, Lee et al. 2009; UMi, Carrera et al. 2002; Leo I, Dolphin 2002; Leo II, Dolphin 2002; and Sagittarius,

de Boer et al. 2015). In Appendix C, we also use the star formation histories of WLM and Aquarius to further test our methodology. We take these from Dolphin (2000) and Cole et al. (2014), respectively. Our full data compilation and derived M_{200}^{abund} and M_{200}^{dyn} for our sample of satellite dwarfs is reported in Table 1.

Finally, in §5.3, we also calculate M_{200}^{abund} estimates for the volume-incomplete sample of ‘ultra-faint’ dwarfs compiled in McConnachie (2012): Segue I, Ursa Major II, Bootes II, Segue II, Wilman I, Coma Berenices, Bootes III, Bootes I, Ursa Major, Hercules, Leo IV, Canes Venatici II, Leo V, Pices II and Canes Venatici I (and see Belokurov et al. 2007; Ibata et al. 2007; McConnachie 2012). Including these ultra-faint dwarfs is complicated by the fact that their star formation histories are more poorly measured than the classical dwarfs. They are also only detectable within the small survey footprint of the Sloan Digital Sky Survey (SDSS), meaning that they are a lower bound on the total number within 280 kpc (e.g. Tollerud et al. 2008). Finally, a large number of dwarfs have recently been found in the Dark Energy Survey (DES) data (Bechtol et al. 2015; Drlica-Wagner et al. 2015; Koposov et al. 2015). However, their uncertain relationship with the Magellanic Group makes it unclear whether or not they should be included in the census of Milky Way dwarfs (Jethwa et al. 2016). To be conservative, we include only those ultra-faints listed above and we apply *no volume completeness correction*. As such, when including the ultra-faints, our subhalo mass function will be

a robust lower bound. Since the SFH of the ultra-faints is poorly constrained, we obtain an upper and lower bound on their $\langle \text{SFR} \rangle$ using equation 2, assuming that they formed all of their stars 0.1 – 1 Gyrs after the Big Bang (Brown et al. 2012; Weisz et al. 2014).

4 THE SIMULATIONS

In §5, we compare our empirically derived cumulative mass function with expectations from Λ CDM using a suite of pure dark matter zoom-in simulations on Milky Way-like galaxies. These simulations are run with the N -body part of GADGET-3, which is an updated version of GADGET-2 (Springel 2005). The simulations are described in detail in Jethwa et al. (2018) but we describe their general properties below.

We select 10 isolated Milky Way-like halos with virial masses between $7.5 \times 10^{11} M_{\odot}$ and $2 \times 10^{12} M_{\odot}$. For each halo, we perform a zoom-in simulation with a particle mass of $2.27 \times 10^5 M_{\odot}$ in the most refined region (enough to resolve subhaloes down to $\sim 5 \times 10^7 M_{\odot}$). We then perform a second zoom-in simulation where a Miyamoto-Nagai disc potential (Miyamoto & Nagai 1975) is grown in the centre of the main halo between $z = 3$ and $z = 1$ (see Jethwa et al. 2018, for more details). The final disk has a mass of $8 \times 10^{10} M_{\odot}$, a scale radius of 3 kpc, and a scale height of 300 pc.

Recent comparisons between cosmological hydrodynamical zoom-ins and dark matter only zoom-ins in which disc potentials are grown have shown that including the disc potential accurately accounts for the destruction of subhalos (Garrison-Kimmel et al. 2017b). Furthermore, Bauer et al. (2018) found that the effect of the disc on substructure is the same if the disc is modelled as a potential or if is simulated with particles and allowed to respond to the substructure. Thus, we have a set of 10 Milky Way-like halos where we can explore the amount of substructure and how it is affected by the inclusion of the disc.

We find that the disc results in a factor of 2 depletion in the amount of substructure within 100 kpc and a factor of 2-4 depletion within 30 kpc (depending on the mass of the main halo). We also find that this depletion is independent of subhalo mass. This suppression of subhalos broadly agrees with full hydrodynamical simulations in Λ CDM (e.g. Sawala et al. 2017; Garrison-Kimmel et al. 2017b) as well as previous works which have grown disks within cosmological simulations (D’Onghia et al. 2010).

5 RESULTS

5.1 Comparing the $\langle \text{SFR} \rangle - M_{200}$ relation with data for nearby isolated and satellite dwarfs

In this section, we test our $\langle \text{SFR} \rangle - M_{200}$ relation by comparing it to data for a sample of 21 nearby dIrr and dSph galaxies, described in §3 and Table 1. Figure 1 shows the $M_* - M_{200}$ relation from Read et al. (2017) (solid blue lines, left) and the $\langle \text{SFR} \rangle - M_{200}$ relation, derived as described in §2.2 (solid blue lines, right). Overplotted are data from the sample of 11 isolated dIrrs taken from Read et al. (2017) (purple data points) and the satellite dwarfs studied in this paper (black data points). The former have their M_{200}^{dyn} derived from their HI rotation curves (Read et al. 2017) and

their $\langle \text{SFR} \rangle$ derived from their stellar masses (equation 1). The latter have their M_{200}^{dyn} and $\langle \text{SFR} \rangle$ determined as described in §2.3 (see also Table 1).

Firstly, notice that most of the satellite dwarfs (black) scatter below the $M_* - M_{200}$ relation (left panel), with the exception of Fornax. Draco and UMi lie more than a dex below, while Sagittarius is off by a factor ~ 3 . This is what we expect if the scatter owes to star formation being quenched on infall, as marked by the red arrow (and see §1). In contrast, the scatter about the $\langle \text{SFR} \rangle - M_{200}$ relation (right panel) is significantly less. Now Sagittarius and UMi lie on the relation within their 68% confidence intervals, while Draco lies just outside the 68% lower bound on its M_{200}^{dyn} . This occurs because dwarfs like Draco have their star formation shut down on infall to the Milky Way, causing their M_* to be systematically low for their pre-infall M_{200} . Their $\langle \text{SFR} \rangle$, however, does not depend on when star formation is truncated and so correlates better with M_{200} than M_* does (see also Appendix C).

While most of the satellites scatter below the $M_* - M_{200}$ relation, Fornax lies significantly above and remains an outlier also in the $\langle \text{SFR} \rangle - M_{200}$ relation (Figure 1). This could indicate that Fornax lost significant mass due to tides. Tidal mass loss lowers M_{200}^{dyn} at a fixed M_{200}^{abund} (see §1). If sufficient mass loss occurs, M_* will start to be lowered also, forming visible tidal tails. To test whether this could explain Fornax’s position in the $M_* - M_{200}$ and $\langle \text{SFR} \rangle - M_{200}$ plots, we consider the Sagittarius dwarf that is known to be tidally disrupting today (Ibata et al. 1995, 1997). The red circle in Figure 1 (left panel) marks the location of Sagittarius in the $M_* - M_{200}$ plot if we use its present-day stellar mass (McConnachie 2012) and M_{200}^{dyn} (we estimate this using Sagittarius’ current stellar kinematics (Ibata et al. 1997) and the Jeans mass estimator from Walker et al. (2009b)). Notice that these ‘present-day’ M_* and M_{200}^{dyn} are lower than our default estimates. This is because our default estimate for M_* corrects for stellar mass loss using Sagittarius’ prominent tidal tails (Niederste-Ostholt et al. 2010, 2012), while our default M_{200}^{dyn} is calculated from the dynamics of Sagittarius stream stars, giving a lower bound on its *pre-infall* halo mass (Gibbons et al. 2017). Thus, for Sagittarius, we see evidence that tides have lowered both its M_{200}^{dyn} and M_* after infall (see the red arrow marked ‘tides’ in Figure 1, left panel). (Indeed, Helmi & White (2001) use dynamical models of Sagittarius disrupting in the Milky Way to show that it likely lost significant mass after accreting onto our Galaxy.) Like Sagittarius, Fornax may have lowered its M_{200}^{dyn} through tides. Note, however, that such an explanation may be challenging to reconcile with Fornax’s apparently near-circular orbit (Lux et al. 2010; Battaglia et al. 2015; Gaia Collaboration et al. 2018) and lack of evident tidal tails (e.g. Bate et al. 2015). We will explore this further in future work.

Finally, there is one more significant outlier in the $\langle \text{SFR} \rangle - M_{200}$ relation (Figure 1, right panel): DDO 154 (marked D154). Uniquely amongst the dIrrs that we consider here, DDO 154 is currently forming stars at four times its $\langle \text{SFR} \rangle$ averaged over a Hubble time (Zhang et al. 2012). It also has an unusually high HI gas fraction of $M_{\text{HI}}/M_* = 37$ (Read et al. 2017). As noted by Read et al. (2017), at its currently observed star formation rate of $\dot{M}_* = 4.3 \times 10^{-3} M_{\odot} \text{ yr}^{-1}$ (Zhang et al. 2012), DDO 154 would move onto the $M_* - M_{200}$ relation in ~ 5.7 Gyrs.

Galaxy	Type	D (kpc)	M_* ($10^6 M_\odot$)	M_{gas} ($10^6 M_\odot$)	$\langle \text{SFR} \rangle$ ($M_\odot \text{ yr}^{-1}$)	M_{200}^{abund} ($10^9 M_\odot$)	M_{200}^{dyn} ($10^9 M_\odot$)	Refs.
UMi	dSph	76 ± 3	0.29	–	2.3×10^{-4}	2.8 ± 1.1	$2.2^{+1.1}_{-0.6}$	3,5
Draco	dSph	76 ± 6	0.29	–	1.2×10^{-4}	1.8 ± 0.7	$3.5^{+1.5}_{-1.0}$	3,4
Sculptor	dSph	86 ± 6	2.3	–	6.8×10^{-4}	5.7 ± 2.3	$3.6^{+1.9}_{-1.4}$	3,6
Sextans	dSph	86 ± 4	0.44	–	1.3×10^{-4}	2.0 ± 0.8	$1.0^{+0.6}_{-0.4}$	3,7
Leo I	dSph	254 ± 15	5.5	–	6.6×10^{-4}	5.6 ± 2.2	$1.8^{+1.2}_{-0.7}$	3,8
Leo II	dSph	233 ± 14	0.74	–	9.8×10^{-5}	1.6 ± 0.7	$1.1^{+0.8}_{-0.4}$	3,8
Carina	dSph	105 ± 6	0.38	–	3.4×10^{-5}	0.8 ± 0.3	$1.2^{+0.7}_{-0.5}$ ($0.4^{+0.4}_{-0.2}$)	3,9,16
Fornax	dSph	138 ± 8	43	–	5×10^{-3}	21.9 ± 7.4	$2.4^{+0.8}_{-0.5}$	3,10
Sagittarius	dSph	26 ± 2	121.5	–	1.7×10^{-2}	50.7 ± 13.3	> 60	3,11,12,14
SMC	dIrr	64 ± 4	460	460	3.3×10^{-2}	77.3 ± 16.9	–	3
LMC	dIrr	51 ± 2	2,700	460	2.0×10^{-1}	198.8 ± 34.3	250^{+90}_{-80}	3,13,15

Table 1. Data for the satellite dwarf galaxies that we study in this work. From left to right, the columns give: the name of the galaxy; type; distance from the centre of the Milky Way; stellar mass; gas mass (for the dIrrs); $\langle \text{SFR} \rangle$, derived using equation 1 for the dIrrs and equation 2 for the dSphs; M_{200}^{abund} derived from the $\langle \text{SFR} \rangle - M_{200}$ relation; M_{200}^{dyn} derived as described in §2.3; and data references. For Carina, M_{200}^{dyn} from the ‘disequilibrium modelling’ analysis of Ural et al. (2015) is quoted in brackets for comparison. The data references for each galaxy are as follows: 1: Read et al. (2017); 2: Dolphin (2000); 3: McConnachie (2012); 4: Aparicio et al. (2001); 5: Carrera et al. (2002); 6: de Boer et al. (2012a); 7: Lee et al. (2009); 8: Dolphin (2002); 9: de Boer et al. (2014); 10: de Boer et al. (2012b); 11: Niederste-Ostholt et al. (2012); 12: de Boer et al. (2015); 13: van der Marel (2006); 14: Gibbons et al. (2017); 15: Peñarrubia et al. (2016); 16: Ural et al. (2015).

This may indicate that it has recently undergone a major merger that increased both its M_{200} and its SFR, but has not yet increased its M_* . Indeed, if we use DDO 154’s current SFR, rather than its $\langle \text{SFR} \rangle$, DDO 154 moves onto the $\langle \text{SFR} \rangle - M_{200}$ relation (see the orange data point in Figure 1 that is connected to DDO 154 by a dashed line).

5.2 Using the $\langle \text{SFR} \rangle - M_{200}$ relation to estimate pre-infall halo masses

In Figure 2, we compare M_{200}^{abund} – derived from the standard $M_* - M_{200}$ abundance matching relation (left), and our new $\langle \text{SFR} \rangle - M_{200}$ relation (right) – with M_{200}^{dyn} for our dwarf sample (see §3). As can be seen, when using standard abundance matching with M_* (left), the satellite dwarfs (black) show a large scatter around the dashed line that marks $M_{200}^{\text{dyn}} = M_{200}^{\text{abund}}$. By contrast, when using our new $\langle \text{SFR} \rangle - M_{200}$ relation (right), the satellites show much less scatter. Now most of the dwarfs – *whether isolated or a satellite* – have a M_{200}^{dyn} and M_{200}^{abund} that agree within their 68% confidence intervals. Only Fornax and DDO154 (discussed in §5.1, above) remain as significant outliers.

As a final check of our methodology, we note that the Carina dSph has an independent estimate of its pre-infall M_{200}^{dyn} from ‘disequilibrium modelling’. Ural et al. (2015) directly fit a large ensemble of N -body models to both its internal stellar kinematic data and extra-tidal stars far from the centre of the dwarf, finding $M_{200, \text{Car}} = 3.6^{+3.8}_{-2.3} \times 10^8 M_\odot$ at 68% confidence. This is in excellent agreement with both the M_{200}^{abund} and M_{200}^{dyn} that we derive for Carina here (see Table 1 and Figure 2).

5.3 The cumulative subhalo mass function of the Milky Way

In this section, we now use our $\langle \text{SFR} \rangle - M_{200}$ relation to obtain an empirical estimate of the subhalo mass function of the Milky Way. For this purpose, we use the volume complete sample of dwarfs within 280 kpc of the Galactic centre, described in §3. We also augment these with a volume-incomplete sample of ‘ultra-faint’ dwarfs. These latter are a lower bound on the number of ultra-faints since we do not perform any volume incompleteness correction, nor do we include any of the new discoveries in the Dark Energy Survey (see §3 for a discussion of these choices).

Figure 3 shows the cumulative pre-infall subhalo mass function of the Milky Way within 280 kpc, derived using our $\langle \text{SFR} \rangle - M_{200}$ relation. The blue lines show the median (solid) and $\pm 68\%$ confidence intervals (dashed) for just the volume-complete classical dwarfs (see §3). The contribution of each dwarf to the cumulative number density is marked by the labels. The green lines show the same but including the sample of ultra-faint dwarfs from McConnachie (2012). (Recall that this is a *lower bound* on the total number of ultra-faints.) The grey shaded region shows the spread in $N(< M_{200})$ of ten pure-dark matter Milky Way zoom simulations in Λ CDM (see §4). The red shaded region shows the same, but including a model for the stellar disc of the Milky Way. This increases the tidal disruption of satellites on plunging orbits causing the subhalo mass function to shift to lower masses (see §4). In both cases, the subhalo masses, M_{200} , are defined to be their peak mass before infall.

From Figure 3, we can see that the cumulative mass

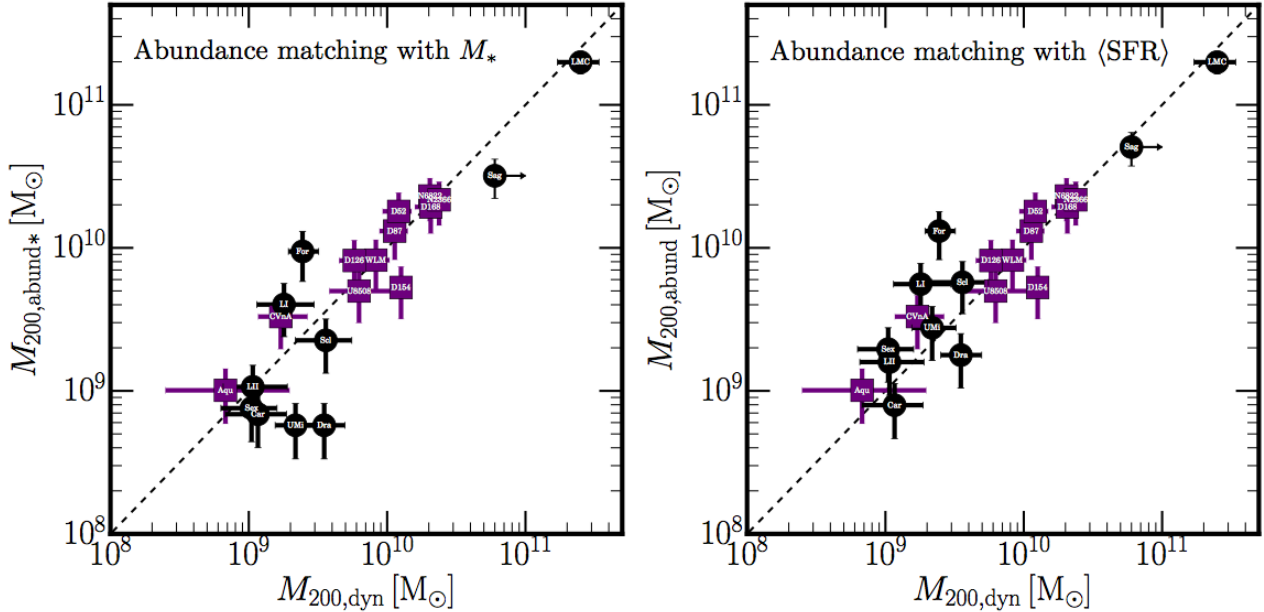


Figure 2. A comparison of the pre-infall M_{200}^{abund} – derived using standard abundance matching with M_* (left), and our new $\langle\text{SFR}\rangle$ – M_{200} abundance matching (right) – with dynamical estimates for nearby galaxies, M_{200}^{dyn} . The purple data points show the sample of isolated star forming dwarf irregulars from (Read et al. 2017); these have their M_{200}^{dyn} estimated from their HI rotation curves. The black points show our sample of Milky Way satellite galaxies (§3). These have their M_{200}^{dyn} estimated as described in §2.3. The dashed line marks $M_{200}^{\text{dyn}} = M_{200}^{\text{abund}}$.

function of Milky Way subhalos agrees excellently with expectations in ΛCDM above $M_{200} \sim 10^9 M_\odot$. This is true if we consider just the Milky Way classical dwarfs (compare the blue lines with the red shaded region), though this would place the Milky Way at the lower end of the range of models we consider here. Including the ultra-faints – that are really a lower bound on the total number of ultra-faints – brings the Milky Way towards the middle of the distribution of models (red shaded region). Notice that the stellar disc of the Milky Way has an important influence, reducing the expected number of subhalos by a factor ~ 2 .

As suggested by independent analyses (e.g. Jethwa et al. 2018), the $\langle\text{SFR}\rangle$ – M_{200} relation suggests that the ultra-faints inhabit dark matter halos with pre-infall halo masses in the range $M_{200} \sim 5 \times 10^8 - 5 \times 10^9 M_\odot$. Below this mass scale, the Milky Way is either truly devoid of visible satellites, or such low mass halos contain just a few tens to hundreds of stars. If this latter is the case, some of these low mass satellites may be detected by the Gaia satellite (e.g. Antoja et al. 2015).

6 DISCUSSION

6.1 Caveats and gremlins

In this section, we discuss the assumptions inherent in our methodology, and likely sources of systematic uncertainty. Firstly, while our sample of classical dwarfs is volume complete down to a given *stellar mass*, this does not mean that it is volume complete down to a given *halo mass*. Thus, we may expect, particularly as we approach $10^9 M_\odot$, that our cumulative mass function is a lower bound, even if using

just the classical dwarfs. Indeed, adding in the sample of ultra-faint dwarfs from McConnachie (2012) we saw exactly this behaviour, with a substantial increase in $N(< M_{200})$ at $M_{200} \sim 10^9 M_\odot$ (compare the blue and green lines in Figure 3). Secondly, we have only tested the $\langle\text{SFR}\rangle$ – M_{200} relation down to $M_{200} \sim 10^9 M_\odot$ (Figure 2). At lower masses than this, there may be substantial scatter in the $\langle\text{SFR}\rangle$ – M_{200} relation that could cause our estimates of M_{200}^{abund} to become biased.

6.2 Comparison with previous work

Recently, Errani et al. (2018) have developed a new mass estimator for dwarf spheroidal stellar systems. They show that their estimator gives an unbiased inference of the mass of subhalos in the Aquarius simulation (a pure dark matter N -body simulation of a Milky Way-mass galaxy in an ΛCDM cosmology; Springel et al. 2008). They then apply it to the Milky Way dSphs to infer their current dynamical masses. In Figure 4, we compare the Errani et al. (2018) dynamical mass estimates with M_{200}^{abund} derived in this paper.

Firstly, note that the Errani et al. (2018) estimator has much larger uncertainties on M_{200}^{dyn} than our GRAVSPHERE estimates (see Figure 2). This is because GRAVSPHERE takes full advantage of the photometric light profile and the second and fourth order moments of the velocity distribution (see §2.3). Nonetheless, the classical dSphs (black data points) broadly agree with our estimates of M_{200}^{abund} within their quoted uncertainties, with the exception of Sagittarius and Fornax. This is in good agreement with our results in Figures 1 and 2, where we found a similar discrepancy for these two dSphs. As discussed previously, for Sagittarius, where

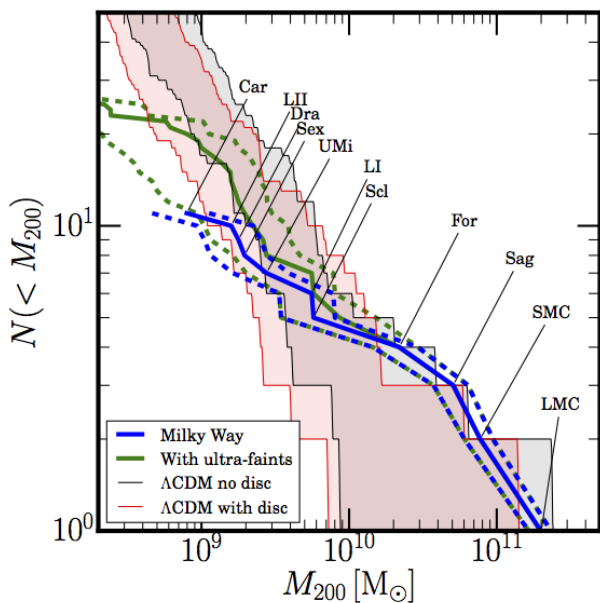


Figure 3. The cumulative subhalo mass function of the Milky Way within 280 kpc of the Galactic centre (blue). The names of the individual galaxies that contribute to the mass function are marked on the plot. The blue dashed lines mark the 68% confidence intervals that include both the uncertainty on M_{200} for each individual galaxy and the error in the $\langle \text{SFR} \rangle - M_{200}$ relation itself. The green lines show the same but including the sample of ultra-faint dwarfs from McConnachie (2012). This is a *lower bound* on the total number of ultra-faints since we have not included the recent DES discoveries, nor accounted for their volume incompleteness within 280 kpc (see §3). The grey shaded region shows the spread in $N(< M_{200})$ of ten pure-dark matter Milky Way zoom simulations in ΛCDM (see §4). The red shaded region shows the same, but including a model for the stellar disc of the Milky Way. In both cases, the subhalo masses, M_{200} , are defined to be their peak mass before infall. Notice that the agreement between our empirically measured mass function, and predictions in ΛCDM is excellent above $M_{200} \sim 10^9 M_{\odot}$.

we have an independent estimate of its pre-infall halo mass from its tidal tails (Gibbons et al. 2017), we showed that this difference between M_{200}^{dyn} and M_{200}^{abund} owes to tidal stripping and shocking lowering its mass after infall. This may also explain the difference between M_{200}^{dyn} and M_{200}^{abund} for Fornax. The ultra-faint dSphs (blue data points) have very large uncertainties on M_{200}^{dyn} . As a result, most are consistent with our M_{200}^{abund} estimates. However, CVnI, Leo IV, Leo V and Hercules all have $M_{200}^{\text{dyn}} < M_{200}^{\text{abund}}$ at 68% confidence. This may indicate that, like Sagittarius and Fornax, these galaxies have had their masses lowered by tidal forces after infall to the Milky Way. We will explore this further in future work.

6.3 Surely abundance matching was always going to work?

The cynical reader may take the view that there are so many dark matter halos predicted in ΛCDM that, given an appropriate mapping between light and dark, abundance matching can always be made to work. Indeed, there are many studies that have shown that such mappings can be found,

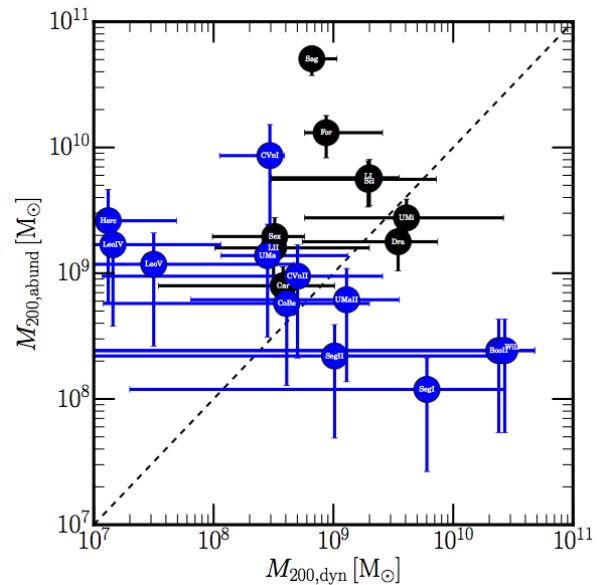


Figure 4. A comparison of M_{200}^{abund} derived in this paper with dynamical masses derived using the mass estimator from Errani et al. (2018). The Milky Way classical dSphs are marked in black, while the ultra-faint dwarfs are marked in blue.

arguing that there is then no missing satellites problem after all (e.g. Madau et al. 2008; Boylan-Kolchin et al. 2012; Brook et al. 2014; Kim et al. 2017). However, what is different here is that we have not set out to solve the missing satellites problem. Rather, we have set out simply to improve abundance matching for quenched galaxies. We introduced a simple new idea that the $\langle \text{SFR} \rangle$ should correlate better with M_{200} for satellites than M_* . We showed empirically that this is the case for a sample of 21 nearby dwarf galaxies (Figure 2). We then applied this idea to a volume complete sample of bright Milky Way satellites within 280 kpc to *measure* the cumulative mass function of bright Milky Way satellites. From this, we showed that there is no missing satellites problem, at least above $M_{200} \gtrsim 10^9 M_{\odot}$. We had no free knobs to push or dials to turn and no part of our analysis was fine-tuned. There is, therefore, nothing trivial about the fact that our derived cumulative mass function is in good agreement with expectations in ΛCDM .

6.4 What about ‘Too Big to Fail’?

Our abundance matching with the $\langle \text{SFR} \rangle$ can be thought of as providing an empirical justification for painting the MW satellites on to the most massive subhalos before infall. Such a mapping has been studied previously in detail and so we know that it produces the correct radial and orbit distribution for the MW classical dSphs (Diemand et al. 2007; Lux et al. 2010), though it may be that the orbits are overly tangential (Lux et al. 2010; Cautun & Frenk 2017). However, a key problem remains. It has long been known that such a mapping predicts central stellar velocity dispersions that are too high to be consistent with the MW classical dSphs (Read et al. 2006b). Boylan-Kolchin et al. (2011) showed that this problem persists for any reasonable mapping be-

tween visible dwarfs and DM subhalos, calling it the “Too Big to Fail” (TBTF) problem.

The etymology of TBTF refers to the fact that it can be solved by an *unreasonable* mapping between light and dark. This requires us to leave some of the most massive subhalos before infall devoid of stars, while simultaneously populating lower mass ones. No physical mechanism that could produce such behaviour has been proposed – the more massive subhalos ought to be “too big to fail” to form stars. However, we have shown here that the MW classical dSphs *do indeed inhabit the most massive subhalos before infall*, consistent with recent analyses that abundance match the satellites directly to simulated subhalos (Jethwa et al. 2018; Kim et al. 2017). In this case, TBTF is really a problem that the central *density* of dwarfs in the Milky Way is lower than expected in pure dark matter Λ CDM structure formation simulations (e.g. Read et al. 2006b; Boylan-Kolchin et al. 2012). This is then identical to the even longer-standing small scale puzzle in Λ CDM: the ‘cusp-core problem’ (Flores & Primack 1994; Moore 1994).

The cusp-core problem refers to the fact that isolated gas rich dwarf irregulars have central dark matter densities that are lower than expected from pure dark matter Λ CDM structure formation simulations. Many solutions to this have been proposed, from modifications to the nature of dark matter (e.g. Spergel & Steinhardt 2000), to bursty star formation physically ‘heating up’ the dark matter, transforming a cusp to a core (e.g. Navarro et al. 1996a; Read & Gilmore 2005; Pontzen & Governato 2012, 2014). Since these solutions act to lower the central densities of dwarf galaxies, they also alleviate the TBTF problem. Indeed, Read et al. (2016) show that if all of the MW dwarfs had a large dark matter core, we would over-solve TBTF and there would not be enough dense dwarfs to explain the data.

Given the intimate connection between the cusp-core and TBTF problems, we will return to both in a forthcoming paper where we measure the internal dark matter densities of a large sample of nearby dIrrs and dSphs (Read et al., in prep. 2018).

6.5 Implications for reionisation

Read et al. (2017) found that the smallest star forming dwarf irregulars like Leo T, Aquarius and CVnIdwA likely inhabit dark matter halos with $M_{200} \lesssim 3 \times 10^9 M_{\odot}$ (Figure 1). Assuming the mean mass growth history in Λ CDM, such halos will have a mass $M_{200} \lesssim 6 \times 10^7 M_{\odot}$ at redshift $z = 7$, when reionisation likely completed (e.g. Hazra & Smoot 2017). This mass scale is in tension with many recent cosmological simulations of isolated dwarfs (see the discussion in Read et al. 2017 and Contenta et al. 2017) and with estimates based on the lack of gas rich faint dwarfs in the ALFALFA HI survey (Tollerud & Peek 2017). Here, we also favour a low host-halo mass for Aquarius, CVnIdwA and Carina. However, interestingly, we favour a similarly low halo mass scale for the gas-free galaxies Leo II and Sextans (see Figure 2) and many of the ultra-faint dwarfs (see Figure 3). The gas-free ultra-faints are substantially more numerous than the classical dwarfs (see the green lines in Figure 3). This may hint at a solution to the puzzle of the low halo masses of Leo T, Aquarius and CVnIdwA: these galaxies may make up some small fraction of galaxies of mass

$M_{200} \sim 1 - 3 \times 10^9 M_{\odot}$, with the rest being ultra-faints that were quenched by reionisation, or some combination of reionisation and ram pressure stripping on infall to the Milky Way (e.g. Gatto et al. 2013). This can occur if this gas-rich subset comprises galaxies that were unusually massive at the epoch of reionisation (e.g. Fitts et al. 2017), or if some process can reignite star formation in a subset of these low mass dwarfs (e.g. Wright et al. 2018). It remains to be seen if such solutions can work in detail.

7 CONCLUSIONS

We have introduced a novel abundance matching technique based on the mean star formation rate $\langle \text{SFR} \rangle$, averaged over the time when a galaxy is forming stars. We compared the masses derived from this relation, M_{200}^{abund} , with direct dynamical estimates for 21 nearby dwarf galaxies, M_{200}^{dyn} , finding excellent agreement between the two (Figure 2). We then used our new $\langle \text{SFR} \rangle - M_{200}$ relation to empirically estimate the cumulative mass function of the Milky Way within 280 kpc of the Galactic centre. Our key results are as follows:

- The cumulative mass function of Milky Way satellites within 280 kpc of the Galactic centre is in good agreement with structure formation simulations in Λ CDM that account for subhalo depletion by the Milky Way disc. We find no evidence for a ‘missing satellites’ problem above $M_{200} \sim 10^9 M_{\odot}$ (Figure 3).
- Our results imply that the Milky Way ‘classical’ dwarfs inhabit dark matter halos with pre-infall masses in the range $M_{200} \sim 10^9 - 10^{10} M_{\odot}$ (Figure 2), while the ‘ultra-faint’ dwarfs inhabit halos with pre-infall masses in the range $M_{200} \sim 5 \times 10^8 - 5 \times 10^9 M_{\odot}$ (Figure 3). This provides a new constraint on cosmological hydrodynamical simulations of the Milky Way and its satellites.
- We find that the lowest-mass gas rich dwarf irregulars – Leo T, Aquarius and CVnIdwA – with $M_{200} < 3 \times 10^9 M_{\odot}$ overlap in mass with the Milky Way classical dwarfs (Figure 2). This implies that either the classical dwarfs had their star formation shut down by ram-pressure stripping on infall to the Milky Way (e.g. Gatto et al. 2013), or reionisation has quenched star formation in only a subset of halos at this mass scale.

Our $\langle \text{SFR} \rangle - M_{200}$ abundance matching method can be readily applied to the dwarf satellites of other nearby spiral galaxies like M31 and Centaurus A. We will consider this in future work.

8 ACKNOWLEDGMENTS

JIR would like to acknowledge support from the STFC consolidated grant ST/M000990/1 and the MERAC foundation. We would like to thank Jorge Peñarrubia for useful feedback on an early draft of the paper.

APPENDIX A: A COMPARISON OF THE SDSS AND GAMA STELLAR MASS FUNCTIONS

In this Appendix, we compare the stellar mass function that we use in this work, that is taken from Behroozi et al.

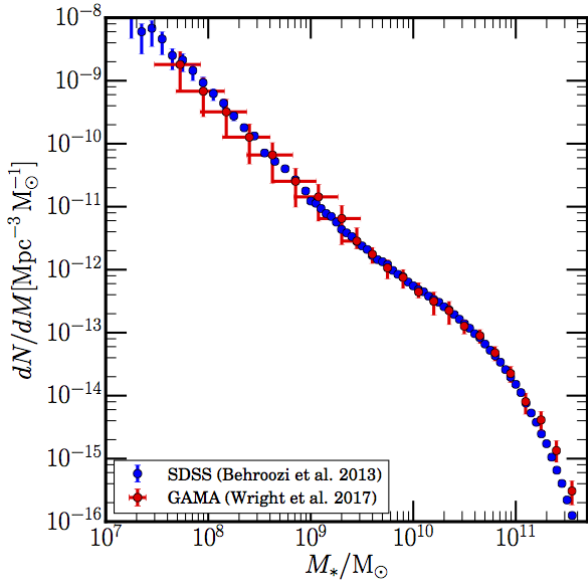


Figure A1. A comparison of the stellar mass function of galaxies in SDSS (blue) and GAMA (red).

(2013) and Baldry et al. (2008) (hereafter the ‘SDSS’ stellar mass function) with the more recent determination from GAMA (Wright et al. 2017). Although GAMA is more recent, the survey volume is substantially smaller than the Blanton et al. (2005) survey on which Baldry et al. (2008) base their stellar mass function (for a discussion on this, see Read et al. 2017). For this reason, the GAMA survey requires some volume correction below $M_* \sim 2 \times 10^9 M_\odot$. To reach to lower stellar mass than this, Wright et al. (2017) combine the GAMA survey results with data from the G10-COSMOS survey (Davies et al. 2015).

In Figure A1, we compare the SDSS (blue) and GAMA (red) stellar mass functions. For the GAMA stellar mass function, we use only volume complete data from GAMA (above $M_* \sim 2 \times 10^9 M_\odot$) and G10-COSMOS (below $M_* \sim 2 \times 10^9 M_\odot$). As can be seen, the GAMA and SDSS stellar mass functions agree within their respective uncertainties. As such, our choice of stellar mass function for this work is not likely to significantly affect our results.

APPENDIX B: THE $\langle \text{SFR} \rangle - M_{200}$ RELATION OVER COSMIC TIME

Ultimately, we want to use the $\langle \text{SFR} \rangle - M_{200}$ relation to calculate pre-infall halo masses for quenched satellites. However, this means applying it at earlier times in the Universe when the $\langle \text{SFR} \rangle - M_{200}$ relation may have been different. If the mean star formation rate depends primarily on halo mass, then to a good approximation we might expect the $\langle \text{SFR} \rangle - M_{200}$ relation to be redshift independent. However, in the early Universe when galaxies are first assembling and star formation rates are much higher than in the Universe today, this assumption may fail (e.g. Behroozi et al. 2013). To test this, we use the $M_* - M_{200}$ relation as a function of redshift derived by Behroozi et al. (2013). In Figure B1, we apply equation 1 to turn this into an $\langle \text{SFR} \rangle - M_{200}$

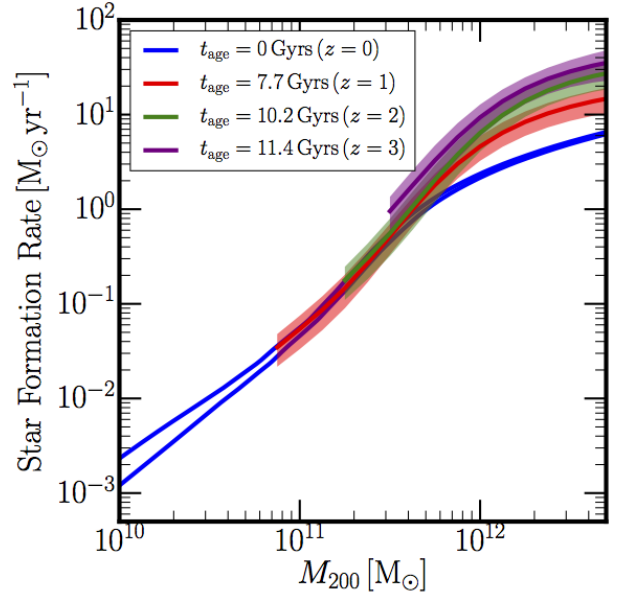


Figure B1. The $\langle \text{SFR} \rangle - M_{200}$ relation as a function of redshift. This is derived from the Behroozi et al. (2013) $M_* - M_{200}(z)$ relations, applying equation 1 to turn these into $\langle \text{SFR} \rangle - M_{200}(z)$ relations. The stellar population age, t_{age} , for each redshift (calculated from the look-back time in ΛCDM) is marked in the legend.

relation as a function of redshift. (Note that when using equation 1, we ensure that the age of the Universe t_{univ} corresponds self-consistently to the redshift at which M_* is measured.) The stellar population age, t_{age} , for each redshift is marked in the legend. As can be seen, the relation remains unchanged within the uncertainties from $z = 0$ to $z = 3$ for $M_{200} \lesssim 3 \times 10^{11} M_\odot$. This is the mass scale of the dwarf satellite galaxies that we are interested in in this work. More massive galaxies, however, show a significant evolution in $\langle \text{SFR} \rangle - M_{200}$, with galaxies at $M_{200} \sim 10^{12} M_\odot$ forming stars at a substantially higher rate in the early Universe than today. Such an effect can be accounted for in the abundance matching and will be important if applying this methodology to massive galaxies falling into galaxy clusters, for example. We will consider this in future work.

APPENDIX C: AN ADDITIONAL TEST OF ABUNDANCE MATCHING WITH THE $\langle \text{SFR} \rangle - M_{200}$ RELATION

As an additional test of abundance matching with the the $\langle \text{SFR} \rangle - M_{200}$ relation, in Figure C1 we derive M_{200} for four nearby dwarfs with well-measured star formation histories: Carina, Fornax, WLM and Aquarius. These have been selected because they all have extended star formation up to at least 2 Gyrs ago (see §3). To test our $\langle \text{SFR} \rangle - M_{200}$ relation, we apply it to each dwarf, artificially truncating their star formation t_{trunc} Gyrs ago. If abundance matching with the $\langle \text{SFR} \rangle - M_{200}$ relation works, then the lines on Figure C1 should be flat, recovering the same M_{200} independently of t_{trunc} . This is indeed the case for Carina, WLM and Aquarius within our quoted uncertainties. Fornax, however, yields a lower M_{200} by a factor ~ 2 if only its old-age stars are

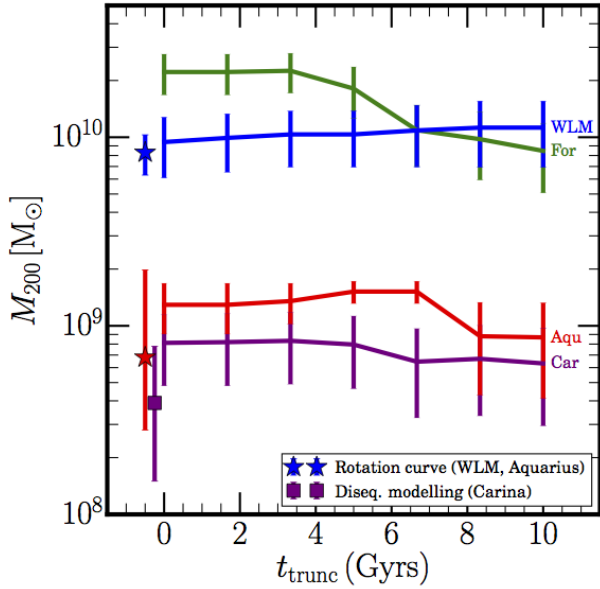


Figure C1. Testing the recovery of the pre-infall M_{200} using our $\langle \text{SFR} \rangle - M_{200}$ abundance matching relation. For this plot, we derive the pre-infall M_{200} for four dwarfs with extended star formation: Carina, Fornax, WLM and Aquarius. We use our $\langle \text{SFR} \rangle - M_{200}$ relation (Figure 1), but artificially truncate the star formation for each dwarf t_{trunc} Gyrs ago. If our abundance matching technique works, then the lines for each dwarf should be flat, recovering the same M_{200} independently of t_{trunc} . This is the case for Carina, WLM and Aquarius within our 68% confidence intervals. Fornax, however, yields a lower M_{200} by a factor ~ 2 if only its old-age stars are used. The stars mark the M_{200} derived from HI rotation curves for WLM and Aquarius (Read et al. 2017). The square marks an independent estimate of the pre-infall M_{200} for Carina from ‘disequilibrium modelling’ (Ural et al. 2015). These are in excellent agreement with the M_{200} derived from the $\langle \text{SFR} \rangle - M_{200}$ relation (see also Figure 2).

used. This could be taken as a measure of the systematic error on M_{200} derived from the $\langle \text{SFR} \rangle - M_{200}$ relation, but a more tantalising possibility is that the rise in the SFR for Fornax actually corresponds to the growth in its M_{200} prior to infall onto the Milky Way. We will consider this further in future work.

REFERENCES

- Antoja T., et al., 2015, MNRAS, 453, 541
Aparicio A., Carrera R., Martínez-Delgado D., 2001, AJ, 122, 2524
Baldry I. K., Glazebrook K., Driver S. P., 2008, MNRAS, 388, 945
Bate N. F., McMonigal B., Lewis G. F., Irwin M. J., Gonzalez-Solares E., Shanks T., Metcalfe N., 2015, MNRAS, 453, 690
Battaglia G., Sollima A., Nipoti C., 2015, MNRAS, 454, 2401
Bauer J. S., Widrow L. M., Erkal D., 2018, MNRAS, 476, 198
Baugh C. M., 2006, Reports on Progress in Physics, 69, 3101
Bechtol K., et al., 2015, ApJ, 807, 50
Behroozi P. S., Wechsler R. H., Conroy C., 2013, ApJ, 770, 57
Belokurov V., et al., 2007, ApJ, 654, 897
Bermejo-Climent J. R., et al., 2018, preprint, (arXiv:1806.07679)
Blanton M. R., Lupton R. H., Schlegel D. J., Strauss M. A., Brinkmann J., Fukugita M., Loveday J., 2005, ApJ, 631, 208
Boylan-Kolchin M., Bullock J. S., Kaplinghat M., 2011, MNRAS, 415, L40
Boylan-Kolchin M., Bullock J. S., Kaplinghat M., 2012, MNRAS, 422, 1203
Brook C. B., Di Cintio A., Knebe A., Gottlöber S., Hoffman Y., Yepes G., Garrison-Kimmel S., 2014, ApJ, 784, L14
Brown T. M., et al., 2012, ApJ, 753, L21
Bullock J. S., Boylan-Kolchin M., 2017, ARA&A, 55, 343
Carrera R., Aparicio A., Martínez-Delgado D., Alonso-García J., 2002, AJ, 123, 3199
Cautun M., Frenk C. S., 2017, MNRAS, 468, L41
Cole A. A., Weisz D. R., Dolphin A. E., Skillman E. D., McConnachie A. W., Brooks A. M., Leaman R., 2014, ApJ, 795, 54
Contenta F., et al., 2017, preprint, (arXiv:1705.01820)
Contreras S., Baugh C. M., Norberg P., Padilla N., 2015, MNRAS, 452, 1861
D’Onghia E., Springel V., Hernquist L., Keres D., 2010, ApJ, 709, 1138
Davies L. J. M., et al., 2015, MNRAS, 447, 1014
Diemand J., Kuhlen M., Madau P., 2007, ApJ, 667, 859
Dolphin A. E., 2000, ApJ, 531, 804
Dolphin A. E., 2002, MNRAS, 332, 91
Drlica-Wagner A., et al., 2015, ApJ, 813, 109
Errani R., Peñarrubia J., Walker M. G., 2018, preprint, (arXiv:1805.00484)
Fattahi A., Navarro J. F., Sawala T., Frenk C. S., Sales L. V., Oman K., Schaller M., Wang J., 2016, preprint, (arXiv:1607.06479)
Fitts A., et al., 2017, MNRAS, 471, 3547
Flores R. A., Primack J. R., 1994, ApJ, 427, L1
Frenk C. S., White S. D. M., Davis M., Efstathiou G., 1988, ApJ, 327, 507
Gaia Collaboration et al., 2018, preprint, (arXiv:1804.09381)
Garrison-Kimmel S., Bullock J. S., Boylan-Kolchin M., Bardwell E., 2017a, MNRAS, 464, 3108
Garrison-Kimmel S., et al., 2017b, MNRAS, 471, 1709
Gatto A., Fraternali F., Read J. I., Marinacci F., Lux H., Walch S., 2013, MNRAS, 433, 2749
Geha M., Blanton M. R., Yan R., Tinker J. L., 2012, ApJ, 757, 85
Gibbons S. L. J., Belokurov V., Evans N. W., 2017, MNRAS, 464, 794
Hazra D. K., Smoot G. F., 2017, preprint, (arXiv:1708.04913)
Hearin A. P., Zentner A. R., Berlind A. A., Newman J. A., 2013, MNRAS, 433, 659
Helmi A., White S. D. M., 2001, MNRAS, 323, 529
Ibata R. A., Gilmore G., Irwin M. J., 1995, MNRAS, 277, 781
Ibata R. A., Wyse R. F. G., Gilmore G., Irwin M. J., Suntzeff N. B., 1997, AJ, 113, 634
Ibata R., Martin N. F., Irwin M., Chapman S., Ferguson A. M. N., Lewis G. F., McConnachie A. W., 2007, ApJ, 671, 1591
Jethwa P., Erkal D., Belokurov V., 2016, MNRAS, 461, 2212
Jethwa P., Erkal D., Belokurov V., 2018, MNRAS, 473, 2060
Katz H., Lelli F., McGaugh S. S., Di Cintio A., Brook C. B., Schombert J. M., 2017, MNRAS, 466, 1648
Kim S. Y., Peter A. H. G., Hargis J. R., 2017, preprint, (arXiv:1711.06267)
Klypin A., Kravtsov A. V., Valenzuela O., Prada F., 1999, ApJ, 522, 82
Koposov S., et al., 2008, ApJ, 686, 279
Koposov S. E., Belokurov V., Torrealba G., Evans N. W., 2015, ApJ, 805, 130
Kravtsov A. V., Berlind A. A., Wechsler R. H., Klypin A. A., Gottlöber S., Allgood B., Primack J. R., 2004, ApJ, 609, 35

- Kravtsov A., Vikhlinin A., Meshcheryakov A., 2014, preprint, ([arXiv:1401.7329](https://arxiv.org/abs/1401.7329))
- Lee M. G., Yuk I.-S., Park H. S., Harris J., Zaritsky D., 2009, *ApJ*, 703, 692
- Lux H., Read J. I., Lake G., 2010, *MNRAS*, 406, 2312
- Macciò A. V., Kang X., Fontanot F., Somerville R. S., Koposov S., Monaco P., 2010, *MNRAS*, 402, 1995
- Madau P., Diemand J., Kuhlen M., 2008, *ApJ*, 679, 1260
- Mandelbaum R., Seljak U., Kauffmann G., Hirata C. M., Brinkmann J., 2006, *MNRAS*, 368, 715
- Mateo M., Olszewski E. W., Walker M. G., 2008, *ApJ*, 675, 201
- Mayer L., Governato F., Kaufmann T., 2008, *Advanced Science Letters*, 1, 7
- McConnachie A. W., 2012, *AJ*, 144, 4
- Mitchell P. D., Lacey C. G., Baugh C. M., Cole S., 2013, *MNRAS*, 435, 87
- Miyamoto M., Nagai R., 1975, *PASJ*, 27, 533
- Mobasher B., et al., 2015, *ApJ*, 808, 101
- Moore B., 1994, *Nature*, 370, 629
- Moore B., Ghigna S., Governato F., Lake G., Quinn T., Stadel J., Tozzi P., 1999, *ApJ*, 524, L19
- Moster B. P., Somerville R. S., Maulbetsch C., van den Bosch F. C., Macciò A. V., Naab T., Oser L., 2010, *ApJ*, 710, 903
- Navarro J. F., Eke V. R., Frenk C. S., 1996a, *MNRAS*, 283, L72
- Navarro J. F., Frenk C. S., White S. D. M., 1996b, *ApJ*, 462, 563
- Niederste-Ostholt M., Belokurov V., Evans N. W., Peñarrubia J., 2010, *ApJ*, 712, 516
- Niederste-Ostholt M., Belokurov V., Evans N. W., 2012, *MNRAS*, 422, 207
- Peñarrubia J., Gómez F. A., Besla G., Erkal D., Ma Y.-Z., 2016, *MNRAS*, 456, L54
- Peacock J. A., Smith R. E., 2000, *MNRAS*, 318, 1144
- Peng Y.-j., et al., 2010, *ApJ*, 721, 193
- Peng Y.-j., Lilly S. J., Renzini A., Carollo M., 2012, *ApJ*, 757, 4
- Percival W. J., 2013, preprint, ([arXiv:1312.5490](https://arxiv.org/abs/1312.5490))
- Planck Collaboration et al., 2014, *A&A*, 571, A16
- Pontzen A., Governato F., 2012, *MNRAS*, 421, 3464
- Pontzen A., Governato F., 2014, *Nature*, 506, 171
- Read J. I., Gilmore G., 2005, *MNRAS*, 356, 107
- Read J. I., Steger P., 2017, *MNRAS*, 471, 4541
- Read J. I., Wilkinson M. I., Evans N. W., Gilmore G., Kleyna J. T., 2006a, *MNRAS*, 366, 429
- Read J. I., Wilkinson M. I., Evans N. W., Gilmore G., Kleyna J. T., 2006b, *MNRAS*, 367, 387
- Read J. I., Agertz O., Collins M. L. M., 2016, *MNRAS*, 459, 2573
- Read J. I., Iorio G., Agertz O., Fraternali F., 2017, *MNRAS*, 467, 2019
- Read J. I., Walker M. G., Steger P., 2018, preprint, ([arXiv:1805.06934](https://arxiv.org/abs/1805.06934))
- Ruiz-Lara T., et al., 2015, *A&A*, 583, A60
- Sawala T., et al., 2016, *MNRAS*, 457, 1931
- Sawala T., Pihajoki P., Johansson P. H., Frenk C. S., Navarro J. F., Oman K. A., White S. D. M., 2017, *MNRAS*, 467, 4383
- Scannapieco C., et al., 2012, *MNRAS*, 423, 1726
- Spencer M. E., Mateo M., Walker M. G., Olszewski E. W., 2017, *ApJ*, 836, 202
- Spergel D. N., Steinhardt P. J., 2000, *Physical Review Letters*, 84, 3760
- Springel V., 2005, *MNRAS*, 364, 1105
- Springel V., Frenk C. S., White S. D. M., 2006, *Nature*, 440, 1137
- Springel V., et al., 2008, *MNRAS*, 391, 1685
- Tollerud E. J., Peek J. E. G., 2017, preprint, ([arXiv:1711.00485](https://arxiv.org/abs/1711.00485))
- Tollerud E. J., Bullock J. S., Strigari L. E., Willman B., 2008, *ApJ*, 688, 277
- Tomozeiu M., Mayer L., Quinn T., 2016, *ApJ*, 827, L15
- Ural U., Wilkinson M. I., Read J. I., Walker M. G., 2015, *Nature Communications*, 6, 7599
- Vale A., Ostriker J. P., 2004, *MNRAS*, 353, 189
- Vale A., Ostriker J. P., 2006, *MNRAS*, 371, 1173
- Walcher J., Groves B., Budavári T., Dale D., 2011, *Ap&SS*, 331, 1
- Walker M. G., Mateo M., Olszewski E. W., 2009a, *AJ*, 137, 3100
- Walker M. G., Mateo M., Olszewski E. W., Peñarrubia J., Wyn Evans N., Gilmore G., 2009b, *ApJ*, 704, 1274
- Walker M. G., Olszewski E. W., Mateo M., 2015, *MNRAS*, 448, 2717
- Weisz D. R., Dolphin A. E., Skillman E. D., Holtzman J., Gilbert K. M., Dalcanton J. J., Williams B. F., 2014, *ApJ*, 789, 147
- Wetzel A. R., Hopkins P. F., Kim J.-h., Faucher-Giguère C.-A., Kereš D., Quataert E., 2016, *ApJ*, 827, L23
- White S. D. M., Rees M. J., 1978, *MNRAS*, 183, 341
- Wright A. H., et al., 2017, *MNRAS*, 470, 283
- Wright A. C., Brooks A. M., Weisz D. R., Christensen C. R., 2018, preprint, ([arXiv:1802.03019](https://arxiv.org/abs/1802.03019))
- Wuyts S., Franx M., Cox T. J., Hernquist L., Hopkins P. F., Robertson B. E., van Dokkum P. G., 2009, *ApJ*, 696, 348
- Zentner A. R., Berlind A. A., Bullock J. S., Kravtsov A. V., Wechsler R. H., 2005, *ApJ*, 624, 505
- Zhang H.-X., Hunter D. A., Elmegreen B. G., Gao Y., Schrubba A., 2012, *AJ*, 143, 47
- Zolotov A., et al., 2012, *ApJ*, 761, 71
- de Boer T. J. L., et al., 2012a, *A&A*, 539, A103
- de Boer T. J. L., et al., 2012b, *A&A*, 544, A73
- de Boer T. J. L., Tolstoy E., Lemasle B., Saha A., Olszewski E. W., Mateo M., Irwin M. J., Battaglia G., 2014, *A&A*, 572, A10
- de Boer T. J. L., Belokurov V., Koposov S., 2015, *MNRAS*, 451, 3489
- van der Marel R. P., 2006, in *The Local Group as an Astrophysical Laboratory*. pp 47–71 ([arXiv:astro-ph/0404192](https://arxiv.org/abs/astro-ph/0404192))